Proceedings of the 21st ICSMGE, Vienna, Austria, 14 – 19 June 2026. Pistrol, Adam & Schweiger (eds.)
Published by: ÖGG, Austrian Society for Geomechanics, Salzburg, Austria, ISBN 978-3-9503898-4-5
https://doi.org/10.53243/ICSMGE2026-792

Finite element modelling of geometrical damping and near-field effects in wave propagation for practical applications

Alireza Esmaeili-Moghadam, Kamelia Atefi-Monfared
Department of Civil Engineering, York University, Toronto, ON, Canada. aliesm@yorku.ca

Giovanni Cascante
Department of Civil and Environmental Engineering, University of Waterloo, Waterloo, Professor, ON, Canada.

ABSTRACT: Geometric damping of ground waves remains challenging in seismology and geotechnical engineering.. While considerable research has examined damping characteristics, (i) extension of near field and P- and R-wave behavior in near field, (ii) and geometrical damping of surface P-waves and Rayleigh waves are unaddressed. This study addresses these gaps using an 8 m × 8 m FEM model with quiet boundaries to represent a semi-infinite medium, verified against Lamb's analytical solution. Wave propagation is simulated numerically, and viscous damping analysis together with advanced signal processing is applied to determine the geometric damping in signals. Previous studies have mainly addressed P-wave geometric damping as body waves and R-waves in the far-field, with limited attention to P- and R-wave damping in the near-field or P-waves on the surface. This study shows that P-wave geometric damping is non-uniform, averaging r^{-1} in the far-field and approximately $r^{-0.4}$ in the near-field—representing about 40% of the far-field value. In the far-field, P-wave velocity aligns with theoretical predictions, whereas in the near-field it is lower in the horizontal and higher in the vertical direction. Viscous damping exhibits frequency dependence: far-field results follow r^{-1}, while near-field responses display low-frequency amplification and high-frequency attenuation, with overall damping reduced by roughly 60% compared to the far-field. For R-waves, far-field damping conforms to the theoretical $r^{-0.5}$ decay, while near-field values are 16% higher in the horizontal and 24% higher in the vertical direction, stabilizing beyond 1.5 m. R-wave velocity converges to theoretical values after 0.5 m—earlier than P-waves—indicating more rapid stabilization in both spatial and frequency domains. Overall, these results clarify the extent and influence of the near field and provide realistic geometrical damping laws for surface P- and R-waves in semi-infinite media, leading to a more robust understanding of surface wave propagation.

KEYWORDS: Geometrical damping, Finite element, Wave propagation, Lamb problem, Near-field.

1 INTRODUCTION

Understanding wave propagation is essential in seismology, geotechnical engineering, and non-destructive testing, where it underpins earthquake analysis, soil response, and structural condition assessment. At low strain levels, surface waves are especially important because they are widely used for soil profile characterization, testing of structural elements, and damage detection. However, existing studies have mainly focused on geometrical damping of P-wave as a body wave in the far field and have not systematically examined P- and Rayleigh-wave geometrical damping and speed of the waves on the surface. Also, the spatial extent of the near-field region where these waves are strongly coupled is unaddressed and no closed-form solution is available for the wave behavior in this range. In this work, we use numerical simulations in a semi-infinite medium to (i) quantify the near-field range and characterize P–R wave behaviour within this mixed region, where surface records do not represent pure P- or pure Rayleigh waves and using such contaminated measurements for NDT can lead to significant errors, and (ii) establish realistic attenuation laws for geometrical damping of P- and Rayleigh waves on the surface and compare them with theoretical expectations, so that practitioners can better select source–receiver offsets and sensor layouts to obtain meaningful signals. The objective of this study is to enhance the physical understanding of surface wave propagation and near-field effects, rather than to provide a design solution for a particular engineering application.

Geometrical damping of the ground can be evaluated using analytical, experimental, or numerical approaches. Analytical methods employ closed-form solutions to quantify damping and attenuation across different wave modes and regions. For example, (Lamb 1904) derived a closed-form solution for Rayleigh wave propagation on the surface in the far-field, while (Woods 1968) linked geometrical damping exponents of $r^{-0.5}, r^{-1}$, and r^{-2} to Rayleigh waves, body P-waves, and surface P-waves, respectively. However, no closed-form solution is currently available for characterizing near-field wave propagation and geometrical damping.

Experimental methods typically deploy accelerometers or geophones at varying distances from the source to record wave-induced vibrations, with damping estimated from the amplitude decay between sensors. While this approach provides practical insight, it can be influenced by noise, equipment errors, and wave reflections.

Numerical modeling offers greater flexibility to simulate complex scenarios, apply varied loading conditions, and mitigate boundary reflections, often at a lower cost than experimental setups. Among these, the Finite Element Method (FEM) has been widely applied to accurately model wave propagation in diverse and intricate environments (Zerwer et al. 2002; Nasseri-Moghaddam 2006; Moghadam and Rafiee-Dehkharghani 2021; Moghadam and Rafiee-Dehkharghani 2022b; Moghadam and Rafiee-Dehkharghani 2022a).

Various signal processing techniques are employed to estimate damping from wave propagation data. These include the spectral ratio method, which evaluates the logarithmic decay of frequency components between two sensor locations, and viscous damping analysis, which uses frequency-domain transforms (e.g., FFT) to quantify attenuation across frequency bands. Time-domain approaches, such as envelope decay analysis or logarithmic decrement methods, can also be used to estimate damping ratios based on amplitude reduction over time or distance.

Several studies have utilized these techniques to assess material and geometrical damping. Aki and Richards (Aki and Richards 2002) applied viscous damping and ratio methods to quantify damping in seismic signals for subsurface characterization. Jiang et al. (Jiang et al. 2011) used ultrasonic pulse velocity (UPV) testing to evaluate hot mix asphalt (HMA) quality, incorporating wave attenuation as a key indicator

alongside velocity. Zerwer et al. (Zerwer et al. 2002) applied viscous analysis of surface waves to profile soils and detect underground structures, using FEM modeling to simulate Rayleigh wave propagation and highlight the role of mesh and attenuation properties. Khan et al. (Khan et al. 2011) developed an ultrasonic method for measuring the damping of stiff geomaterials, addressing challenges like equipment delays.

Existing literature has extensively examined the damping characteristics of body and surface waves in the far-field. However, a significant gap remains in the analysis of geometrical damping specific to P-waves and Rayleigh waves on the surface, particularly in the near-field. The commonly cited r^{-2} geometrical damping for surface P-waves actually corresponds to head waves, not to the P-waves detected on surface signals. Moreover, the near-field geometrical damping and speed of both P- and R-waves is largely unaddressed, and the spatial extent of the region where these waves are strongly coupled and cannot be treated as separate phases, are largely unaddressed. Previous studies have primarily considered P-waves as body waves and have often neglected surface-propagating P-waves and their distinct geometrical damping on the ground surface. These gaps in the literature are partly due to the challenges of accurately modeling surface wave propagation and isolating individual wave modes for damping analysis. In this context, finite element modeling provides a powerful tool for investigating and quantifying near-field geometrical damping with high spatial and temporal resolution.

In our study, an accurate FEM model is modelled and verified with Lamb analytical solution. We then focus on two main objectives: (i) quantifying the near-field range and characterizing P–R wave behaviour within this mixed region, where surface records do not represent pure P- or pure Rayleigh waves, and (ii) establishing realistic geometrical damping laws for P- and Rayleigh waves on the surface in both the near and far field, and comparing them with theoretical expectations. P- and R-wave contributions in the FEM signals are separated using a Tukey window, and their geometrical and viscous damping are evaluated over different spatial ranges. The results show that the P-wave displacement on the surface decays approximately as r^{-1}, rather than r^{-2}, indicating slower geometrical damping and a more persistent P-wave contribution at the surface than commonly assumed. The aim is to improve the physical understanding of surface wave propagation, near-field effects, and geometrical damping at low strain levels, so that wave-based tests for soil characterization and structural damage detection can be better planned and interpreted, rather than to provide a design solution for a specific engineering application.

Section 2 reviews wave propagation theory, FEM modeling considerations, and viscous and geometrical damping. Section 3 describes the study methodology, and Section 4 presents FEM model verification against the Lamb analytical solution.

2 THEORY AND BACKGROUND

Wave propagation in solid dry ground is governed by the principles of elastic wave theory, where waves propagate through the material by inducing deformations in the medium. The fundamental equation governing the propagation of elastic waves in solid dry ground is the linear elastic wave equation, which describes the relationship between stress and strain in the material.

2.1 *Wave Propagation in Solid Dry Ground*

Wave propagation in dry ground under small-strain elasticity is governed by:

$$\mu\nabla^2 u + (\lambda + \mu)\nabla e + F = \rho\ddot{u} \tag{1}$$

where μ and λ are Lamé constants, e is dilatation, F is external force, and ρ is density. Finite element simulations are performed in COMSOL Multiphysics with spatial discretization constrained by the smallest wavelength $\lambda_{min} = V_R/f_{max}$ and at least 10 elements per wavelength to minimize numerical dispersion (Lysmer and Kuhlemeyer 1969; Virieux 1986; Holberg 1987). Temporal discretization satisfies both the Nyquist criterion, $\Delta t < 1/(2f_{max})$, to avoid aliasing, and the Courant–Friedrichs–Lewy (CFL) condition, $\Delta t \leq C\Delta x/V_p$, to ensure stability (Kim and Bathe 2016). A Courant number of $C = 0.175$ is adopted based on prior studies (Zerwer et al. 2002; Nasseri-Moghaddam 2006; FLAC3D [no date]).

2.2 *Viscous damping calculations*

Viscous damping describes how wave amplitude decreases with frequency as a signal propagates through a medium. Unlike time-domain damping, it captures frequency-based attenuation. Since no physical damping is applied in this model, the viscous damping reflects only geometrical damping across frequencies. The viscous damping ratio can be calculated as a function of frequency, $D(f)$, utilizing the Fourier transform of two pulse echoes, $A_1(f)$ and $A_2(f)$, as follows(Khan et al. 2011):

$$D(f) = \frac{1}{\Delta\phi}\ln\left(\frac{A_1(f)}{A_2(f)}\right) \tag{2}$$

Where $\Delta\phi$ is the difference of phase angle between the first and second signal.

2.3 *Geometrical Damping*

Geometrical damping refers to the amplitude reduction of seismic waves as their wavefronts expand with distance from the source. In the far-field, Rayleigh waves confined to the surface decay as $r^{-0.5}$ due to cylindrical spreading, while body P- and S-waves decay as r^{-1} from spherical spreading (Woods 1968).

These theoretical decay exponents serve as reference values in this study to assess the damping behavior of both P- and R-waves in the near-field and far-field. Deviations from these values can indicate complex interactions, such as surface–body wave coupling or near-field effects, which are examined in section 5. The schematic of wave spreading for body waves and surface waves is shown in Figure 1.

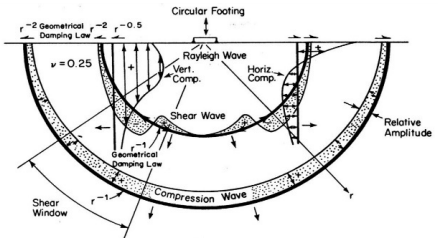

Figure 1. Wave propagation spreading of P-, S-, and R-wave (Woods 1968)

3 METHODOLOGY

In this study, wave propagation in a solid elastic medium is simulated using COMSOL Multiphysics. Model validity is verified by comparing FEM results with the analytical solution of Lamb (Lamb 1904). A surface displacement $f-k$ plot is then generated to confirm the absence of numerical dispersion. The Tukey window is applied to isolate the P-wave and R-wave components of the FEM results, after which their geometrical

and viscous damping are evaluated over different spatial ranges and compared with theoretical predictions.

4 VERIFICATION

In this study, Lamb's analytical solution (Lamb 1904) serves as a benchmark for validation. Lamb's analysis primarily concentrated on computing the far-field vertical and horizontal displacement histories originating from a point source generating Rayleigh waves on an infinite half-space. The precise analytical solution for Rayleigh wave displacements is meticulously elaborated by Ba˚th and Berkhout (Båth 2013).

For verification of the FEM model, an 8m × 8m model has been developed utilizing the material properties detailed in Table 1. The Lamb parameters employed for this analysis are as follows: $Q_0 = 1\,N.s$, $\tau = 0.00075s$, and $t_0 = 0.036s$, and the loading function and the FFT of it is depicted in Figure 2.

Table 1. Material properties of the ground

Parameter	Value
Density ρ (Kg/m^3)	1600.0
Modulus of Elasticity E (MPa)	19.0
Poisson ratio v	0.2
Shear Modulus G (MPa)	7.92
P-wave velocity V_p (m/s)	114.9
S-wave velocity V_s (m/s)	70.3
Rayleigh wave velocity V_R (m/s)	64.1

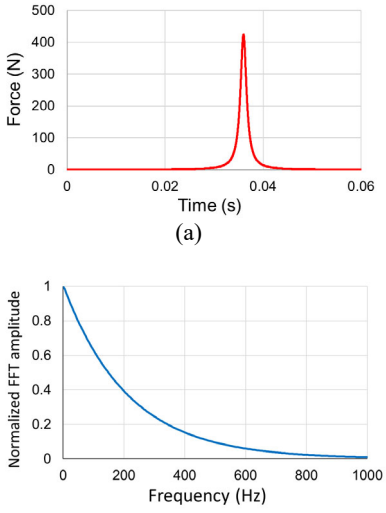

Figure 2. (a) Force function (b) Normalized FFT of force

Frequency analysis shows that 97.5% and 50% of the content lie below 800 Hz and 150 Hz, respectively. Accordingly, 800 Hz is used as the maximum meaningful loading frequency for mesh size selection, and 150 Hz is used to estimate the near-field extent (0–1.5 m) based on $2\lambda_p$. Using 10 elements per minimum wavelength yields an 8 mm mesh size. To improve computational efficiency, graded meshing is applied with a 1% vertical growth rate, while maintaining a uniform 8 mm horizontal mesh. Smaller (8 mm) elements are placed near the surface, and larger (8.7 cm) elements at the model base. Quiet boundaries are applied to reduce wave reflections. The mesh configuration is shown in Figure 3.

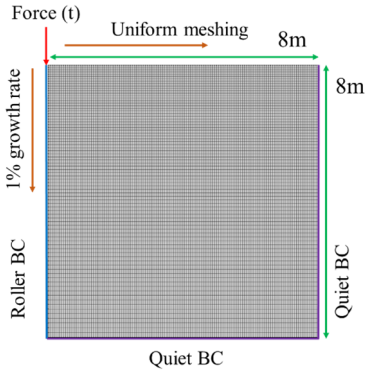

Figure 3. Schematic figure of the modelling

In this paper, results are illustrated only for the horizontal direction; however, vertical direction results are also discussed. For P-waves, only horizontal results are analyzed in detail, as their primary displacement occurs in the horizontal direction.

For verification, horizontal; displacements 3m and 6m away from the loading (along the surface) are compared with the closed form solution for R-wave and illustrated in Figure 4.

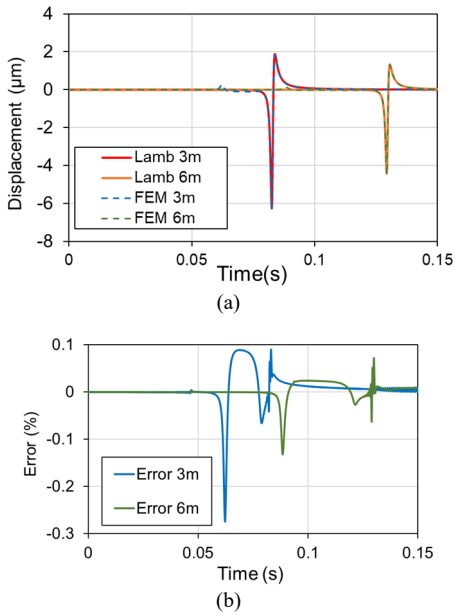

Figure 4. (a) FEM vs. Lamb solutions at 3 m and 6 m for horizontal displacement; (b) error between Lamb and FEM horizontal displacement results.

The error between the FEM simulation and the closed-form solution is less than 4% for horizontal and 2.5% for vertical direction, primarily due to the FEM model capturing the full wavefield, including body waves, whereas Lamb's closed-form solution accounts only for the Rayleigh wave component.

5 RESULTS AND DISCUSSION

5.1 *2D-FFT of the results and f-k plot*

In this section, the presence of numerical dispersion in the model is assessed by generating the f-k plot of the horizontal displacement on the surface, spanning from 1m to 6m with a sampling distance of 5cm and illustrated in Figure 5.

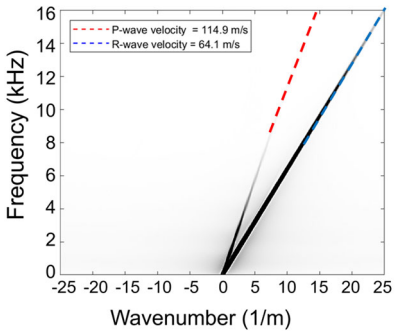

Figure 5. f-k plot of the horizontal displacement on the surface from the FEM

The f-k plot of the numerical results is illustrated in Figure 5 indicates the lack of bending at higher frequencies, indicating the absence of numerical dispersion. Additionally, the f-k plot of the FEM results reveals no reflections in the time history of the waves within this frequency range. The f-k plot of the FEM results shows both P-wave and R-wave effectively.

5.2 *Wave speed in space*

In this section, P- and R-wave's speeds are calculated in space. The R-waves and P-waves are first isolated using a Tukey window, after which their arrival times are identified. Wave velocities are then computed at various locations. R-wave and P-wave speeds in horizontal direction are presented in Figure 6.

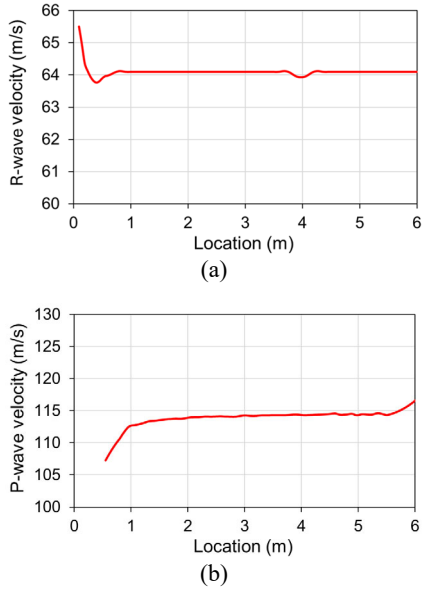

Figure 6. Determined (a) R-wave velocity (b) P-wave velocity from spatial variation of horizontal displacement signals.

The R-wave's speed in near-field is different from theoretical value and after 1m, the wave speed is the same as the theory for horizontal and vertical direction. Additionally, the detected R-wave speed in near-field in vertical displacements' signals are smaller than theoretical value, but in horizontal displacements' signals are larger than theory.

In the near-field, P-wave speed deviates from the theoretical value—being lower in horizontal displacement signals and higher in vertical ones. Within 0–1 m of the source, the measured speed differs significantly from theory, but converges gradually beyond 1.5–2 m. After 5 m, boundary effects cause increased noise. Vertical displacement signals are noisier than horizontal, as surface P-waves predominantly induce horizontal motion; the minimal vertical component, mainly from the Poisson effect, is sensitive to numerical noise.

5.3 *R-wave geometrical damping*

In this section, the geometric damping of the R-wave extracted from the FEM results is examined. Initially, the R-wave within the FEM signals is isolated using a Tukey window. Subsequently, the maximum horizontal and vertical displacements in space and viscous damping are presented.

5.3.1 *Damping of the R-wave amplitude in space*

To demonstrate the damping of the maximum amplitude of the R-wave across space, the R-wave is first isolated from the entire FEM signal using a Tukey window. Subsequently, the maximum amplitude of the R-wave, spanning from 0.1m to 1.5m (near-field range), and 1.5m to 6m (far-field range), with a sampling rate of 5cm, derived from FEM solution, along with the regression function corresponding to the maximum displacements. The maximum horizontal R-wave displacement and its far-field regression are shown in Figure 7.

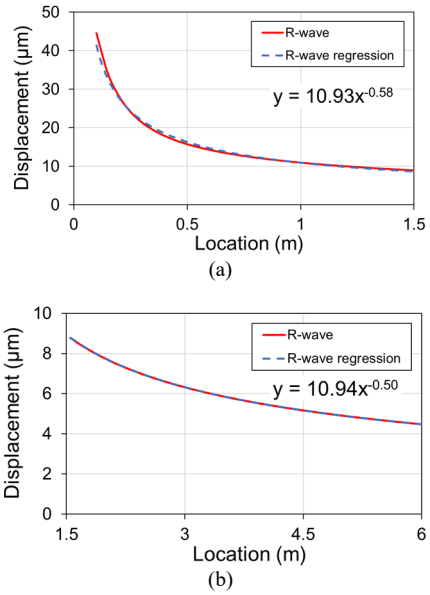

Figure 7. Maximum horizontal R-wave displacement from FEM results: (a) near-field, (b) far-field.

The geometrical damping of the R-wave in the near-field is $r^{-0.58}$ in the horizontal direction and $r^{-0.62}$ in the vertical direction as shown in Figure 7. These values are 16% and 24% higher than the theoretical far-field value of $r^{-0.50}$ for the vertical and horizontal directions, respectively. Additionally, the vertical damping in the near-field is greater than the horizontal damping. The geometrical damping of the R-wave in both horizontal and vertical directions in the far-field, as shown in Figure 7, aligns with the theoretical value of $r^{-0.5}$. These findings validate the FEM model's ability to accurately capture geometrical damping effects. The spatial geometrical damping of the R-wave in the horizontal direction is shown in Figure 8.

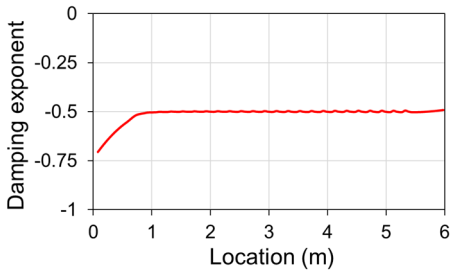

(a)

Figure 8. Spatial damping of R-wave for horizontal displacement.

The results suggest that in the far-field, the geometrical damping in both horizontal and vertical directions aligns with the theoretical $r^{-0.5}$ decay. However, in the near-field, the observed damping is higher than expected. The vertical component converges to the theoretical value beyond 1.5 m from the source, whereas the horizontal component reaches this value earlier, at approximately 1 m.

5.3.2 *Viscous damping of R-wave*

Next, the viscous damping of the R-wave is computed for both near- and far-field cases, in vertical and horizontal directions, and compared with theoretical predictions. Far-field analysis uses signals at 2 m and 4 m, while near-field analysis uses signals at 0.9 m and 1.05 m. As no physical damping is included in the FEM model, the observed viscous damping across frequencies reflects only the effects of geometrical damping. The near-field and far-field viscous damping of the R-wave in the horizontal direction is shown in Figure 9.

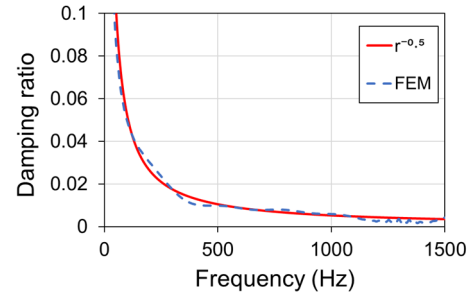

(a)

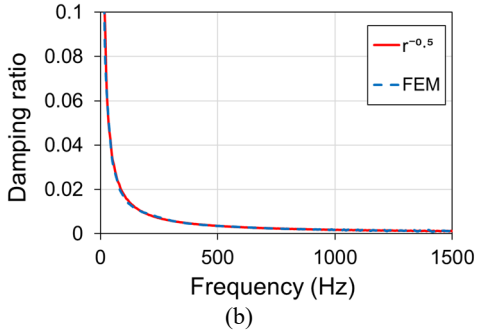

(b)

Figure 9. Viscous damping of R-wave from FEM horizontal displacement vs. theory: (a) near-field , (b) far-field.

Results indicate that R-wave damping on the surface in the far-field, for both horizontal and vertical directions, agrees with theoretical predictions across frequencies, confirming consistency with analytical solutions. In the near-field (0.90–1.05 m), damping values are close to theory but deviate more than in the far-field. Near-field damping also shows greater frequency dependence, though it remains broadly consistent with theoretical expectations.

5.4 *P-wave geometrical damping*

This section will analyze the geometric damping of the P-wave derived from the FEM results. Initially, the P-wave is isolated from the FEM signals using a Tukey window. Following this, the presentation will include the maximum horizontal and vertical displacements in space, P-wave speed in space, and viscous damping of P-wave.

5.4.1 *Damping of the P-wave amplitude in space*

To examine spatial damping of the maximum P-wave amplitude, P-waves are isolated from the FEM signal using a Tukey window. Maximum amplitudes are then extracted at 5 cm intervals from 0.85–1.5 m (near-field) and 1.5–6 m (far-field). Vertical displacement is excluded as surface P-waves exhibit only horizontal displacement. The 0–0.85 m range is omitted because the P-wave is not fully developed. The horizontal displacement in both near- and far-field regions, along with its regression, is shown in Figure 10.

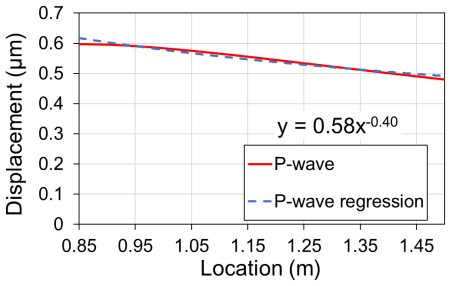

(a)

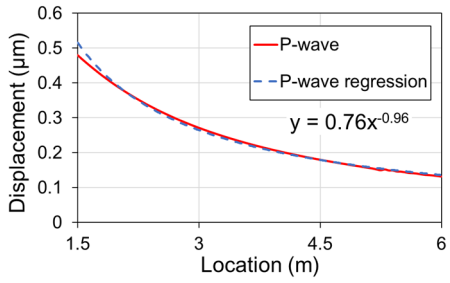

(b)

Figure 10. Maximum horizontal P-wave displacement from FEM: (a) 0.85–1.5 m, (b) 1–6 m.

From the FEM simulation, the regression exponents for horizontal displacement are −0.40 in near-field and −0.96 in far-field. Thus, near-field geometrical damping is about 40% of that in the far-field. The far-field P-wave damping closely matches that of a body wave, indicating that the detected P-wave results from body–surface interaction rather than a head wave, which would exhibit r^{-2} damping.

The geometrical damping of P-wave in space is computed and illustrated in Figure 11.

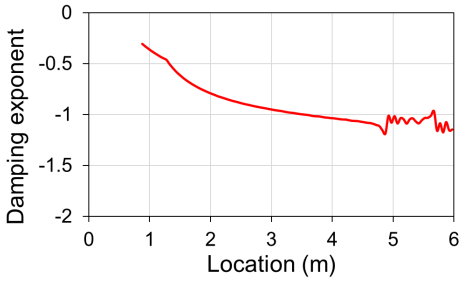

Figure 11. The damping of P-wave in space

The results in Figure 11 indicate that the geometrical damping of the P-wave is significantly lower in the near-field compared to the far-field. Additionally, the damping exponent varies between the range of 0.8 to 1.2, centering around 1.

5.4.2 *Viscous damping of P-wave*

In the subsequent step, the viscous damping of the horizontal displacement of P-wave signal between 0.9m-1.05m as near-field and 2m-4m as far-field are illustrated in Figure 12.

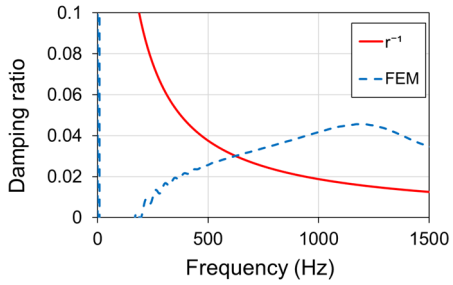

(a)

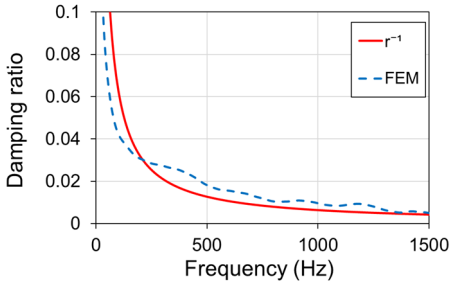

(b)

Figure 12. Viscous damping of P-wave from FEM horizontal displacement vs. theory: (a) near-field , (b) far-field.

Figure 12 shows that near-field P-wave damping is more variable and frequency-dependent than in the far-field, with amplification at low frequencies (0–250 Hz) and higher damping than theoretical values at 750–1500 Hz. On average, it is lower than the theoretical r^{-1} prediction in near field, consistent with Figure 11 and Figure 10. Far-field damping aligns with r^{-1} in average but is lower at low frequencies and higher at high frequencies. Unlike relatively constant R-wave damping, P-wave damping is frequency-dependent.

6 ACKNOWLEDGEMENT

This research was supported by the Natural Sciences and Engineering Research Council of Canada (NSERC).

7 CONCLUSION

This study theoretically investigates the geometrical damping of P- and R-waves from a point source on the ground using a finite element (FEM) model and the analytical Lamb solution. After reviewing geometrical damping theory and Lamb's formulation, an FEM model of wave propagation in a semi-infinite medium is developed, verified against Lamb's solution, and used to separate P- and R-waves with a Tukey window so their geometrical damping can be computed and compared with theory. Whereas previous research has mainly treated P-waves as body waves and R-waves in the far field, with little attention to near-field P–R behaviour or surface P-wave geometrical damping, this study examines (i) wave behaviour and the extent of the near field and (ii) surface geometrical damping in both the near and far field. This study finds P-wave geometric damping to be non-uniform between adjacent spatial signals: averaging r^{-1} in the far-field (matching theory) and $r^{-0.4}$ in the near-field (40% of far-field value). P-wave velocity converges to theory in the far-field but is lower horizontally and higher vertically in the near-field. Viscous damping analysis shows that in the far-field, P-waves have lower damping at low frequencies and higher at high frequencies compared to theory, with the average matching r^{-1}. In the near-field, low frequencies show amplification (negative damping), high frequencies show greater attenuation, and overall viscous damping is below r^{-1}. R-wave far-field geometric damping matches $r^{-0.5}$; in the near-field, it exceeds theory by ~16% horizontally and ~24% vertically, stabilizing beyond 1.5 m. In the frequency domain, far-field viscous damping is uniform and consistent with $r^{-0.5}$, while near-field values average close to theory but show greater frequency variation. R-wave velocity reaches theory beyond 0.5 m, compared to 1.5 m for P-waves. These results confirm R-wave characteristics stabilize faster than P-waves.

8 REFERENCES

Aki, K. and Richards, P.G. 2002. *Quantitative seismology*.

Båth, M. 2013. *Mathematical Aspects of Seismology: Developments in Solid Earth Geophysics*. Elsevier.

FLAC3D. [no date]. *https://docs.itascacg.com/flac3d700/flac3d/docproject/source/options/dynamic/formulation/formulation.html*.

Holberg, O. 1987. Computational aspects of the choice of operator and sampling interval for numerical differentiation in large-scale simulation of wave phenomena. *Geophysical prospecting* 35(6), pp. 629–655.

Jiang, Z., Ponniah, J., Cascante, G. and Haas, R. 2011. Nondestructive ultrasonic testing methodology for condition assessment of hot mix asphalt specimens. *Canadian Journal of Civil Engineering* 38(7), pp. 751–761.

Khan, Z., Cascante, G. and El Naggar, M.H. 2011. Measurement of dynamic properties of stiff specimens using ultrasonic waves. *Canadian Geotechnical Journal* 48(1), pp. 1–15.

Kim, K.-T. and Bathe, K.-J. 2016. Transient implicit wave propagation dynamics with the method of finite spheres. *Computers & Structures* 173, pp. 50–60.

Lamb, H. 1904. I. On the propagation of tremors over the surface of an elastic solid. *Philosophical Transactions of the Royal Society of London. Series A, Containing papers of a mathematical or physical character* 203(359–371), pp. 1–42.

Lysmer, J. and Kuhlemeyer, R.L. 1969. Finite dynamic model for infinite media. *Journal of the engineering mechanics division* 95(4), pp. 859–877.

Moghadam, A.E. and Rafiee-Dehkharghani, R. 2021. Optimal design of wave barriers in dry and saturated poroelastic grounds using Covariance Matrix Adaptation Evolution Strategy. *Computers and Geotechnics* 133, p. 104015.

Moghadam, A.E. and Rafiee-Dehkharghani, R. 2022a. Ground-borne vibration screening in layered dry and saturated grounds using optimal inclined wave barriers. *Soil Dynamics and Earthquake Engineering* 162, p. 107448.

Moghadam, A.E. and Rafiee-Dehkharghani, R. 2022b. Wave barriers for mitigation of underground train vibrations in the layered grounds considering the groundwater table effect. *Construction and Building Materials* 348, p. 128629.

Nasseri-Moghaddam, A. 2006. Study of the effect of lateral inhomogeneities on the propagation of Rayleigh waves in an elastic medium.

Virieux, J. 1986. P-SV wave propagation in heterogeneous media: Velocity-stress finite-difference method. *Geophysics* 51(4), pp. 889–901.

Woods, R.D. 1968. *Screening of suface waves in soils*.

Zerwer, A., Cascante, G. and Hutchinson, J. 2002. Parameter estimation in finite element simulations of Rayleigh waves. *Journal of geotechnical and geoenvironmental engineering* 128(3), pp. 250–261.